ARTICLE OPEN

Hydrogen bonding interactions of H₂O and SiOH on a boroaluminosilicate glass corroded in aqueous solution

Dien Ngo[1,2], Hongshen Liu[1,2], Zhe Chen [1,2], Huseyin Kaya[3], Tawanda J. Zimudzi [2], Stéphane Gin [4], Thiruvillamalai Mahadevan[5], Jincheng Du [5] and Seong H. Kim[1,2,3*]

Hydrogen bonding interactions play an important role in many chemical and physical processes occurring in bulk liquids and at interfaces. In this study, hydrous species (H₂O and Si-OH) on nano-porous alteration layers (gels) formed on a boroaluminosilicate glass called International Simple Glass corroded in aqueous solutions at pH 7 and pH 9, and initially saturated with soluble silicon-containing species were analyzed using linear and non-linear vibrational spectroscopy in combination with molecular dynamics simulations. The simulation results revealed various possible types of hydrogen bonds among these hydrous species in nanoconfinement environments with their populations depending on pore-size distribution. The nano-porous gels formed on corroded glass surfaces enhance hydrogen bond strength between hydrous species as revealed by attenuated total reflectance infrared spectroscopy. Sum frequency generation spectroscopy showed some significant differences in hydrogen bonding interactions on alteration layers formed at pH 7 and pH 9. The glass dissolution under the leaching conditions used in this study has been known to be ten times faster at pH 7 in comparison to that at pH 9 due to unknown reasons. The simulation and experimental results obtained in this study indicate that the water mobility in the gel formed at pH 9 could be slower than that in the gel formed at pH 7, and as a result, the leaching rate at pH 9 is slower than that at pH 7.

INTRODUCTION

Borosilicate glass has been used as a host matrix for radioactive wastes in the nuclear industry due to its good processability, chemical durability, radiation stability, and high-load capacity.[1–3] However, during its storage in repository locations, nuclear waste glass could get into contact with underground water, if the repository is damaged, leading to aqueous corrosion of glass and release of radioactive elements into the geosphere.[4–6] Nuclear glass corrosion occurs at a rate on the order of 0.1–1 μm/day at 90 °C in the first stage (Stage-I) and then it gradually slows down due to the formation of an alteration layer on the surface and the increase of solution concentrations of network former and modifier species being released from the glass matrix.[6,7] The corrosion process enters the second stage (Stage-II) when the corrosion solution is saturated with respect to soluble silicon-containing species.[8] It would be ideal if the corrosion process remains in this stage until the radioactive decay of the nuclear waste diminishes to the safe level. The corrosion rate in Stage-II is limited mainly by the transport of mobile species within the nano-porous alteration layer,[7,9] especially diffusion of water and solvated ionic species. To understand the mechanism of glass corrosion in the second stage, it is therefore very important to obtain information on interfacial behaviors of hydrous species (molecular water and Si-OH) on the alteration layer; particularly, hydrogen bonding interactions between these species are expected to affect the transport of water molecules in the alteration layer.

Transport properties and hydrogen bonding interactions of hydrous species in the nano-porous materials have been investigated using various analytical techniques and computational simulations.[10–33] Computational studies showed that transport and hydrogen bonding interactions can be significantly altered by the confinement in nanoscale geometry.[9,21,34–36] The alteration layer formed on glass upon corrosion in aqueous solution has been shown to be nano-porous and transport of water within the layer has been characterized in some experimental studies.[37–43] One of the most efficient methods to probe hydrogen bonding interactions of hydrous species is vibrational spectroscopy, especially infrared (IR) and sum frequency generation (SFG) spectroscopy. That is because the OH stretch band is very sensitive to the strength of hydrogen bonding interactions.[44,45] While IR spectroscopy has been used to study the ingress of water into glass surface upon leaching/corroding in aqueous solution, only changes in total amount of hydrous species were considered in most studies.[46–51] For hydrous species at interfaces, SFG has been shown to be a powerful tool.[44,45,52] To the best of our knowledge, there are only two reports studying hydrous species on glass surfaces leached in pH 1 aqueous solutions using SFG spectroscopy.[47,48] In these studies, however, the porous structure of leached layer was unknown and only hydrous species in non-centrosymmetric medium (a medium without an inversion center) were analyzed. A comprehensive study of the alteration layer combining elemental analysis, pore-size characterization, and analysis of hydrogen bonding interactions of hydrous species (H₂O and SiOH) in both centrosymmetric and non-centrosymmetric media is critically needed to understand aqueous glass corrosion mechanism and transport of molecular water and other mobile species within the nano-porous alteration layer.

In this study, X-ray photoelectron spectroscopy (XPS) and spectroscopic ellipsometry (SE) were used to determine the chemical composition, porosity and pore-size distribution, as well

[1]Department of Chemical Engineering, The Pennsylvania State University, University Park, PA 16802, USA. [2]Materials Research Institute, The Pennsylvania State University, University Park, PA 16802, USA. [3]Department of Materials Science and Engineering, The Pennsylvania State University, University Park, PA 16802, USA. [4]CEA, DEN, DE2D, Université de Montpellier, Marcoule, France. [5]Department of Materials Science and Engineering, University of North Texas, Denton, TX 76203, USA. *email: shkim@engr.psu.edu

as thickness of the alteration layers formed on a model nuclear waste glass called International Simple Glass (ISG)[53] corroded in aqueous solutions of pH 7 and pH 9 at 90 °C for short (7 days) and long (2046 days) durations. The former pH condition is representative of a granitic-type aquifer and the latter condition corresponds to the pH buffered by boron species released from the glass.[38,54] Attenuated total reflectance infrared (ATR-IR) spectroscopy and SFG spectroscopy were then used to study hydrogen bonding interactions on these layers. Molecular dynamics (MD) simulations were performed to better understand the effects of pore size on hydrogen bond length distributions in nano-porous gels. Results from XPS show that elemental compositions of alteration layers formed in solutions at different pH values are quite similar, while SE results reveal an increase in pore size with corrosion time in aqueous solutions. ATR-IR spectroscopy shows the dominance of solid-like hydrous species (strongly hydrogen-bonded hydrous species) in the alteration layers and SFG spectroscopy reveals some differences in hydrogen bonding interactions on ISG corroded at pH 7 and pH 9. The results from various techniques in this study provide a better understanding of hydrous species on the alteration layers that would further improve our understanding of glass corrosion mechanism.

RESULTS AND DISCUSSION

XPS depth profile

The thickness and depth profiles of alteration layers formed on ISG samples corroded for 7 days and 2046 days in silica-saturated solutions at pH 7 and pH 9 are given in Table 1 and Fig. 1, respectively. The results show that the thicknesses of altered layers on ISG corroded for 7 days and 2046 days in pH 7 solutions are ~750 nm and ~2400 nm, respectively. The alteration layers on ISG corroded for 7 days and 2046 days in pH 9 solutions, however, are much thinner in comparison to those on ISG corroded in pH 7 solutions for the same corrosion times. They are only ~150 nm and ~300 nm for 7-day- and 2046-day-corroded samples, respectively. These thickness values reveal that the initial corrosion rate of ISG, as well as the steady-state thickness of the alteration layer in silica-saturated solution are much lower at pH 9 than pH 7.[38,54] The alteration layers in Fig. 1 show the nearly complete depletion of Na and B, and the retention of Ca, which is consistent with the previous literature.[42,55] The added electrolyte (K^+ in this study) in the corrosion solution can ingress into the alteration layer and the type of electrolyte also affects the retention of Ca in the layer.[42] The Zr and Al concentrations are lower near the surface than in the deeper region and this is due to the higher concentration of O at the surface. The fact that the Al/Si ratios in the alteration layer and the bulk are very close to each other (except near the external surface) could mean two possibilities—either congruent dissolution or no dissolution of Al and Si into the corrosion solutions used in this study. Since the aqueous solution was initially saturated with soluble silica-containing species, the latter is expected to be the case; but, if the speciation of soluble silica changes,[56,57] then a limited dissolution of Si is also possible at the beginning of the

corrosion treatment. Furthermore, the gel is in a local minimum according to a thermodynamic point of view and it could undergo hydrolysis/condensation reactions to reach a more stable state.[58]

The elemental compositions of alteration layers formed on ISG samples corroded in solutions at different pH values in this study are very similar as revealed in Fig. 1 (see also Supplementary Figs 1 and 2 in the SI). The samples were prepared at the same time and treated in the same environmental conditions for the same duration, except the solution pH and K^+ ion concentration; the factors contributing to such stark differences in corrosion rate and alteration layer thickness at these pH conditions are not well known.[38,54] An understanding of this difference would help design glass and corrosion conditions with better corrosion resistance.

Porosity and pore-size distribution of alteration layers

Information on porosity and pore-size distribution of alteration layers is very important to understand the glass corrosion process in aqueous solutions. Water transport, dynamics, and structure in nano-porous materials have been shown to be different from those in the bulk.[9,20,21,32,59] It was shown for alteration layers formed on ISG corroded in aqueous solutions that there is an evolution of pore size in the layers with corrosion time and it is accompanied by a structural rearrangement of the alteration layer.[9,40] In consequence, the transport and behavior of water and mobile elements would change with the evolution of alteration layer and they need to be considered in theoretical modeling and computational simulation of glass corrosion.

Ellipsometric angles (Ψ and Δ) and optical models of ISG samples corroded for 7 days and 2046 days in silica-saturated solutions at pH 7 and pH 9 are given in Fig. 2. The ellipsometric angles and optical models were determined for the samples at 0% relative humidity (RH). During the drying process at 0% RH, physisorbed water molecules in open pores are desorbed. The optical models at 0% RH estimate thickness, void and solid volume fractions of the alteration layers.[40] The SE results show that the thickness of alteration layer determined from SE is comparable to that determined from XPS depth profiling (see Table 1). The porosity values of the thickest sublayers of alteration layers given in Fig. 2 are comparable within the experimental uncertainty, and they are also comparable to the porosity of the gel formed in the presence of K^+ ions as reported by Collin et al.[42] The SE models at 0% RH also revealed a non-uniformity of the alteration layer in terms of porosity, which is congruent with the previously reported literature.[38–41]

Humidity-dependent SE experiments were then performed to determine average pore size and pore-size distribution (when possible) in the alteration layers.[40] The water adsorption isotherms at room temperature (~22 °C) and pore-size (diameter) distribution of alteration layers are given in Fig. 3. The ISG samples corroded for 7 days at pH 7 and pH 9 show type-I isotherm indicating that the average pore sizes in the alteration layers on these samples are much smaller than 2 nm.[60] The isotherms of 2046-day-corroded samples show type-IV isotherm with some hysteresis due to capillary condensation; then, the pore sizes were calculated using the Kelvin equation.[40,60] The pore-size distributions of alteration layers on these samples were determined by taking the first derivative of water volume fraction versus the pore diameter. The pore network structure of alteration layer is unknown, thus both branches of the hysteresis loop were used for calculations of pore-size distributions.

The shapes of type-IV isotherm on two ISG samples corroded for 2046 days are different. This means that the pore fractions, pore sizes, and pore inter-connections are different in the two alteration layers.[61,62] The pore-size distributions in Fig. 3 reveal that there is a higher population of large pores (>2 nm) in the pH 7, 2046-day-corroded layer in comparison to that in the pH 9, 2046-day-corroded layer. This difference in pore-size distribution can lead to a difference in transport properties of water and

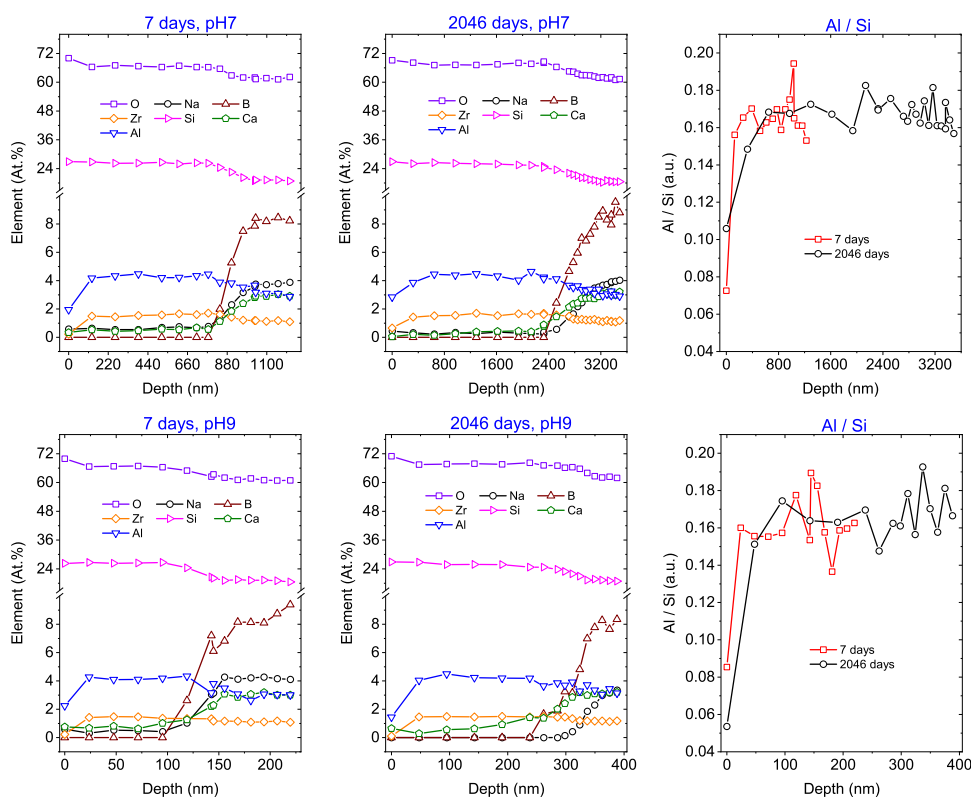| Table 1.	Alteration layer thickness on corroded ISG coupons.	
Samples	Thickness by XPS (nm)	Thickness by SE (nm)
7 days, pH 7	750	725 ± 24
7 days, pH 9	150	177 ± 3
2046 days, pH 7	2400	2049 ± 8
2046 days, pH 9	300	278 ± 5

The uncertainty in XPS depth profiling is ~10%

Fig. 1 XPS depth profiles of the original network former and modifier species in ISG glass corroded for 7 days and 2046 days in silica-saturated solutions at pH 7 and pH 9.

mobile species in these alteration layers, and it may be one of the factors contributing to higher corrosion rate of ISG in solutions at pH 7 than pH 9 (Figs 1 and 2).

The size of pores in alteration layers formed on ISG glass and other glasses corroded in aqueous solutions has been reported in several studies using different analytical techniques.[38–41,63] Kinosita measured humidity-dependent refractive index of surface layers formed on acid treated dense flint and dense crown glasses and found the presence of pores with a mean pore radius from 6 to 23 Å. Using transmission electron microscopy (TEM), Gin et al.[39] observed a 10 μm thick microporous layer with a range of pore diameter from 10 to 170 nm on a SON68 glass block corroded for 25.75 years in granitic groundwater at 90 °C and 100 bar. The presence of a layer with ~1 nm pore on ISG corroded in aqueous solutions for <1 year was also reported.[38,41] The evolution of pore size in alteration layer of ISG with corrosion time in aqueous solution up to 1625 days was demonstrated by Ngo et al.[40] using humidity-dependent spectroscopic ellipsometry. The pore-size distribution on ISG sample corroded for 2046 days in the same conditions is very different from that on 1625-day-corroded sample (see Supplementary Fig. 3 in the SI). It means that the gel layer was still continuously reorganizing when the ISG sample was kept in the solution for a longer time.[9] The nano-porous structure of alteration layer suggests that transport of mobile species and hydrogen bonding interactions in the layer would deviate from those in bulk liquid water and they would change with the evolution of alteration layer during the corrosion process in aqueous solution.

MD simulations of hydrogen bonds in nano-porous silica gels

The pore structure of the alteration layer is very complicated with a distribution of pore sizes.[64] The interactions between pore wall (consisting of silanol and siloxane groups) and molecular water, as well as between water molecules within the nanopores can result

in the formation of various types of hydrogen bonding interactions in the nano-porous alteration layer. MD simulations were performed to investigate different types of hydrogen bonds in nano-porous gel structures with the backbone aluminosilicate glass having the composition of 76.8% SiO_2, 14.4% Al_2O_3, and 8.8% CaO (in mole%). The MD simulations revealed the presence of various types of hydrogen bonds and their characteristic bond length distributions.

Figure 4 shows two most abundant and one minor types of hydrogen bonds (HBs) and corresponding hydrogen bond length (O···HO) distributions in nano-porous silica gels of different pore sizes generated at various temperatures in simulations (see Fig. 9 in the Methods for pore-size distributions). Other minor HB types and bond length distributions can be found in the Supplementary Information (Supplementary Fig. 5). The MD simulation results in Fig. 4 show that HBs can be formed between water molecules in pores, between silanol groups and the water molecules, and between the water molecules and siloxane bridging oxygen (BO) group. The different normalizing factors in the plots indicate that the most probable value of the HB length distribution changes with pore size.

For the HBs between water molecules, the average HB length at all pore sizes is ~1.80 Å, which is close to that of bulk water.[34] However, there is a slight shift in the distribution of HB length in the Gel298 to the shorter length indicating that the population of stronger HBs between water molecules increases with a decrease in the pore size. The water molecules are closer due to the limited space.

For the case of HBs between the oxygen of water and the hydrogen of SiOH (silanol), the average HB length is ~1.72 Å, which is less than that between water molecules in the pores. This indicates that the HB of water molecule with the silanol group at the internal surface is stronger than the HB between two water molecules. Furthermore, the distribution of HB lengths in Gel298 is
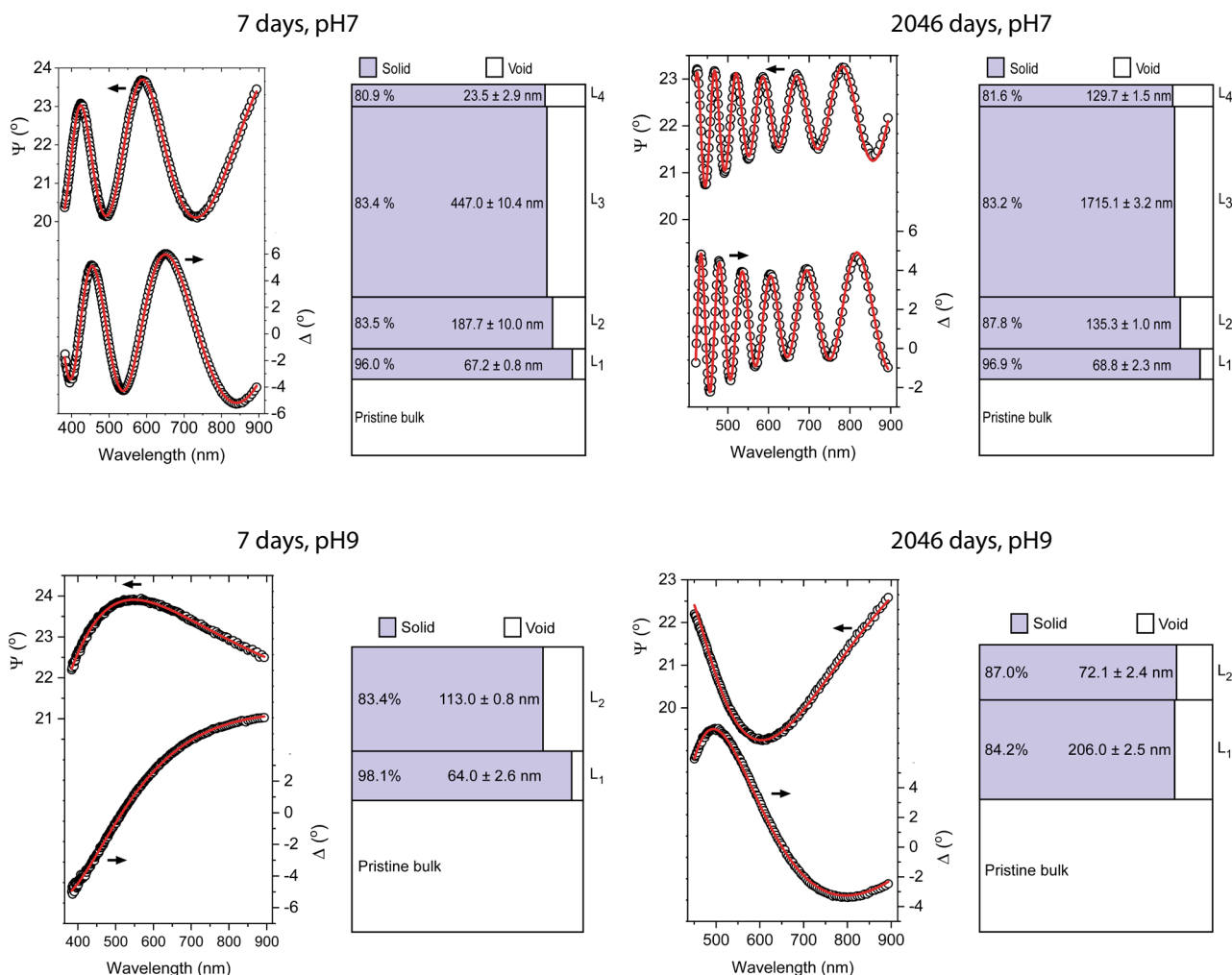
Fig. 2 Ellipsometric angles Ψ and Δ and optical models of ISG samples (on the right of each angle plot) corroded for 7 days and 2046 days in silica-saturated solutions at pH 7 and pH 9. The angles and optical models correspond to the samples at 0% RH.

slightly shifted to the longer distance relative to that in Gel398 and Gel598. This shift means that the fraction of water molecules having weaker HB interactions with SiOH groups at the internal surface of pores increases when pores are smaller.

The average HB length between the BO atom and the hydrogen of water (~1.90 Å) is significantly longer than the HB lengths in the two previous cases. This type of HB was considered to be responsible for the SFG vibrational mode centered at ~3660 cm^{-1} at the silica/water interface in the study by Cyran et al.[65] The layer of "surface water", which has structure and dynamics different from that of bulk liquid water can be as thick as 0.9 nm (~3 monolayers);[21,66] thus for pore diameter of <2 nm, the hydrogen bonding interactions occur mostly between hydrous species with "surface" characteristics.

The HB length distributions of hydrous species inside nanopores of the alteration layer provide critical information needed for spectral interpretation of the OH stretching vibrations. It is well known the OH stretch band position is a function of the HB strength. Figure 5 is a reproduction of the empirical as well as theoretical relationship between the OH stretch peak position and the O⋯HO distance.[67–69] Based on the HB length distribution found in the MD simulations, the molecular water species hydrogen bonding to each other (Fig. 4a) are expected to produce a broad OH stretch band centered at 3400–3500 cm^{-1}. The silanol group hydrogen bonded to molecular water (Fig. 4c) will produce a band centered at 3200–3300 cm^{-1}; this band would

be even broader than the band at 3400–3500 cm^{-1} because the O⋯HO distance dependence of the peak position is larger in this strongly hydrogen-bonded region. The water molecules hydrogen-bonded to the siloxane BO atom (Fig. 4e) will produce a narrower band around 3500–3680 cm^{-1}. However, it should be noted that due to the broad distribution of the O⋯HO distance (Fig. 4b, d, f), the OH stretch bands of these hydrogen-bonded species will overlap significantly. Thus, without knowing the exact distribution of hydrogen bonding interactions, it would be difficult to do quantitative deconvolution of the experimental spectra into various hydrous species. For example, the two hydrogen-bonded silanol groups (Supplementary Fig. 5a) and the silanol group hydrogen bonded to a siloxane BO atom (Supplementary Fig. 5e) can also produce broad bands near 3400–3500 cm^{-1}, although their contributions would be small due to lower probability (Supplementary Fig. 5b, f) compared to the hydrogen-bonded molecular water species (Fig. 4b). The water molecules donating the hydrogen to the silanol oxygen atom (Supplementary Fig. 5c) can also contribute to the band near 3500–3680 cm^{-1}. A very weak hydrogen bonding interactions (for example, with the O⋯HO distance longer than 2 Å) will induce only a minor red-shift of the OH peak mode from the free-OH stretch position (3740 cm^{-1}).

Hydrogen bonding interactions between surface silanol and water at the silica/water interface have been studied extensively through MD simulations.[34,70–73] The HB lengths at a neat water/silica interface and electrolyte/silica interfaces were calculated and
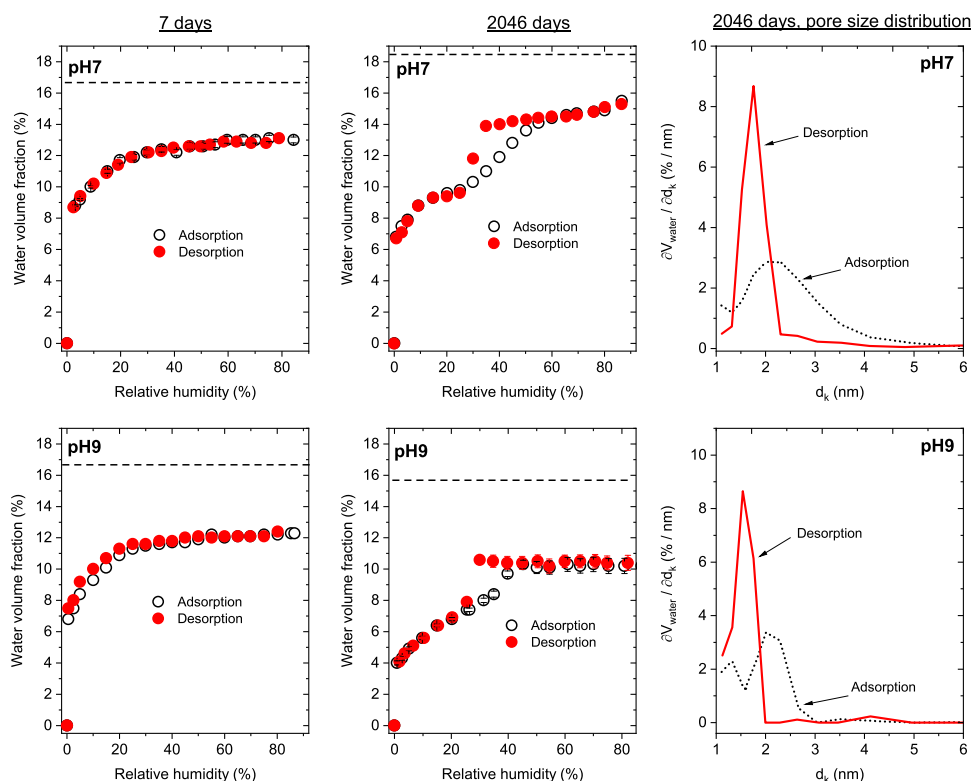
Fig. 3 Water adsorption isotherms on ISG samples corroded for 7 days and 2046 days in silica-saturated solutions at pH 7 and pH 9. The isotherms are for layer 3 (thickest layer) on pH 7-corroded samples, and for layer 2 and layer 1 on pH 9-corroded samples for 7 days and 2046 days, respectively. Pore-size (diameter) distributions were calculated for 2046-day-corroded samples using both branches of the hysteresis loop. The 90% confidence intervals from the ellipsometry data analysis are shown in isotherm plots; but most of them are smaller than the symbol size.

the results showed that the intra-surface HB between silanol and silanol is weakened significantly when electrolytes are present at the interface.[73] This study also showed that the perturbing effect of cation adsorption on interfacial properties is stronger than that of anion adsorption.[71] The acidity of surface silanol groups varies with the type of electrolyte present at the interface.[72] The results in these studies were obtained for flat silica/water interface; however, hydrogen bonding interactions could be further complicated when effects of confined geometry are considered. The MD simulations in the present study were performed without electrolyte ions in the pores while alteration layers in real applications would contain mobile ion species.[42] Further simulation studies including electrolytes in nanopores therefore are needed to provide a better understanding of hydrogen bonding interactions of hydrous species in the alteration layer.

ATR-IR spectra of hydrous species in the alteration layer

Alteration layers on corroded ISG samples were shown to be nano-porous with larger pore sizes on samples corroded for a longer time in aqueous solutions. ATR-IR spectroscopy was used to obtain vibrational spectra of all hydrous species in these porous layers. The spectra were measured at ~37% RH and are given in Fig. 6a. At this relative humidity, about 3/4 of the void volume fraction of alteration layer determined at 0% RH condition is filled with molecular water and capillary condensation and evaporation are occurring on 2046-day-corroded samples (see Fig. 3). The IR spectra of hydrous species in the alteration layers are quite similar although their thicknesses are significantly different.

ATR-IR spectroscopy is a linear optical technique and spectral intensity or integrated peak area is proportional to the amount of detected species within the probing volume. Figure 6a shows that at 37% RH, the amount of hydrous species detected within the

ATR-IR probing volume is the largest for the ISG sample corroded for 7 days at pH 7 and the smallest for the one corroded for 7 days at pH 9. In ATR-IR, the penetration depth (d_p) for the squared evanescent field[74] is ~118 nm at 3400 cm^{-1} and then a probing depth was considered to be ~354 nm ($3d_p$ at 3400 cm^{-1}) in this study. This probing depth is comparable to the thickness of alteration layer on 2046-day-corroded ISG at pH 9, larger than that on 7-day-corroded ISG at pH 9, and much smaller than the thickness of alteration layer on samples corroded for 7 days and 2046 days at pH 7. The spectral signal on the 7-day-corroded sample at pH 9 is lowest because the alteration layer thickness is less than the probing depth. The spectral signals on 2046-day-corroded ISG at pH 7 and pH 9 are comparable within the experimental uncertainty. These samples have pores with diameter larger than 2 nm and this makes capillary evaporation possible at 37% RH (see Fig. 3). The 7-day-corroded sample at pH 7 has no capillary evaporation at 37% RH (see Fig. 3) and its alteration layer thickness is larger than ATR-IR probing depth and has a porosity comparable to other three samples (see Fig. 2 and Table 1); as a result, this sample has a spectral signal higher than that of 2046-day-corroded samples. In real applications, corroded sample might be exposed to dry cycles between fully immersed periods in aqueous solutions, and adsorption and desorption of molecular water could make porous alteration layers susceptible to sorption-induced deformation.[75] The stability of alteration layer therefore could be reduced. The deformation of alteration layer with respect to changes in relative humidity and solution conditions (pH, electrolyte concentration, type of electrolyte, etc.) is under investigation and will be presented elsewhere.

Mid infrared (Mid-IR) spectroscopy has been used to study confined water.[28,76–81] Boissière et al.[76] studied confined water in lamellar structures of bis (2-ethylhexyl) sulfosuccinate sodium salt
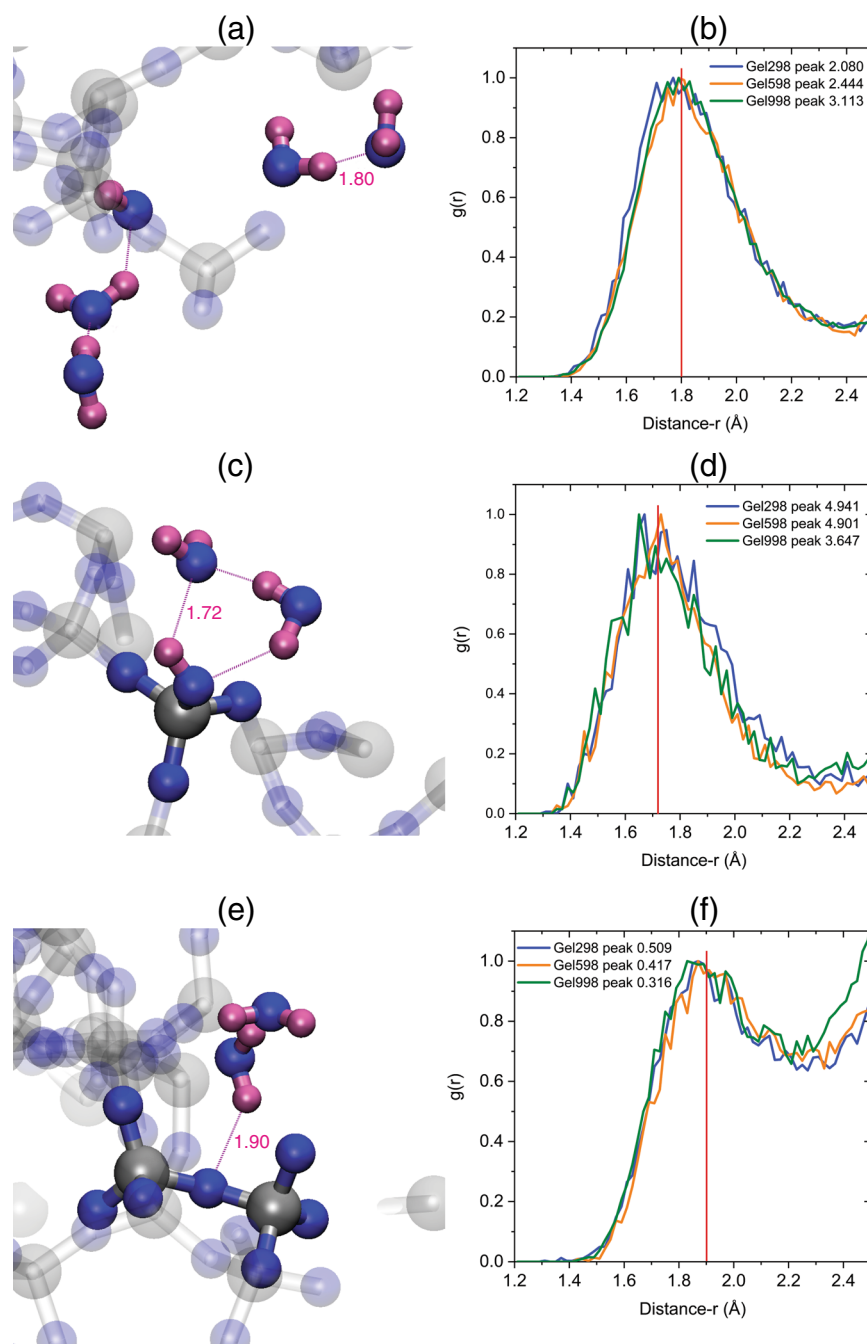
Fig. 4 Molecular dynamics simulations of hydrogen bonds of hydrous species in nano-porous silica gels. a MD snapshot of hydrogen bonds between oxygen of water and hydrogen of the nearby water ($O_{water} \cdots H_{water}$) and **b** $O_{water} \cdots H_{water}$ bond length distribution. **c** MD snapshot of hydrogen bonds between oxygen of water and hydrogen of the nearby SiOH ($O_{water} \cdots H_{silanol}$) and **d** $O_{water} \cdots H_{silanol}$ bond length distribution. **e** MD snapshot of hydrogen bonds between hydrogen of water and oxygen of the nearby siloxane ($O_{siloxane} \cdots H_{water}$), and **f** $O_{siloxane} \cdots H_{water}$ bond length distribution. The HB length distributions were normalized to the peak populations given in the plots. Gel298, Gel598 and Gel998 correspond to the nano-porous structures generated at 298, 598, and 998 K, respectively. The blue, purple, and gray balls represent the oxygen, hydrogen, and silicon atoms, respectively.

(AOT) surfactants using Mid-IR spectroscopy and fitted the OH stretch band using three Gaussian peaks. The three peaks are ~3320 cm^{-1}, 3465 cm^{-1}, 3585 cm^{-1}, and they are named as "network" water, "intermediary" water, and "multimer" water, respectively. In the study of water confined in NaA zeolites (sodium form of the Linde Type A zeolite) using Mid-IR spectroscopy, Crupi et al.[28] deconvolved the obtained spectra into three components at ~3290 cm^{-1}, 3470 cm^{-1}, and 3590 cm^{-1}. The

authors could then monitor the change in contribution of three components to the overall spectrum upon temperature changes.

The ATR-IR spectra in this study were also fitted using three Gaussian peaks following the approach described above.[28,76] During the spectral deconvolution, all fitting parameters were allowed to vary due to different porous structures of these corroded samples. Figure 6b shows the spectral fitting of ISG sample corroded for 7 days at pH 7. ATR-IR spectra (except the
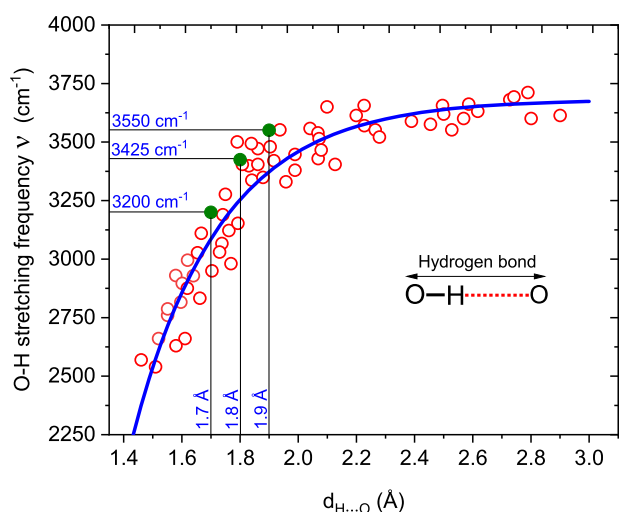
Fig. 5 **Relationship between O–H stretching frequency and H···O distance in solid materials.** The raw data were taken from refs [67–69]. The olive symbols and black solid lines show examples of the correlation between the O–H stretching frequency and H···O distance. The blue solid line is the fitting of raw data.

spectrum of 7-day-corroded sample at pH 9) could be fitted to three peaks centered at ~3270 cm^{-1}, 3470 cm^{-1}, 3600 cm^{-1} (see Supplementary Table 1 in the SI). The spectrum of 7-day-corroded sample at pH 9 could still be fitted with three Gaussian peaks; however, due to the lower signal to noise ratio of this spectrum, the fitting was less accurate and the three peak centers are at lower wavenumbers in comparison to those of other samples. From MD simulation results, the peak centered at ~3270 cm^{-1} could be assigned to SiOH hydrogen bonded to water and the one centered at ~3470 cm^{-1} could be attributed to water species hydrogen bonded to each other (Fig. 4a, c). Hydrogen bonds between water and oxygen on siloxane group (Fig. 4e) could account for the peak centered at ~3600 cm^{-1}. As noted above, however, the hydrogen bond length distribution is broad so that the vibrational bands of these hydrous species overlap significantly. Figure 6c shows the normalized integrated areas of peaks obtained from spectral deconvolutions. The results reveal that peak 1 (~3270 cm^{-1}) has the highest percentage in all corroded samples, indicating the dominance of strongly hydrogen-bonded hydrous species in alteration layers containing nanopores. The percentages of peak 1 on pH 7-corroded samples appear to be slightly higher than those on pH 9-corroded ones; however, it should be noted that the fitting of a poorly resolved broad band with multiple component is always subject to a large error. Thus, small differences among the fit results would not have any significant meaning. Overall, based on the peak position and relative abundance of these three components, one can say that most hydrous species in these nano-porous alteration layers are strongly hydrogen-bonded to each other.

Hydrous species on glass and porous samples have been investigated in other studies using ATR-IR spectroscopy.[46–50,82–84] It has also been used to study the state of confined water with/without the presence of electrolytes.[19,81,85] The water ingress into the glass surface upon leaching and corrosion in aqueous solutions was clearly demonstrated by an increase in the signal intensity of hydrous species after experiments.[48,49] The SiOH/H$_2$O ratio was found to be related to the glass composition and silicate network structure,[50,86] and this ratio could be determined by a combination of ATR-IR spectroscopy and hydrogen depth profiling.[50] Information on the SiOH/H$_2$O ratio with corrosion time in aqueous solution would support a better understanding of the glass corrosion mechanism.

SFG spectra of hydrous species
ATR-IR spectroscopy was used to obtain vibrational spectra of hydrous species in the alteration layers and the spectra obtained show quite similar hydrogen bonding interactions in the alteration layers formed on ISG samples corroded for 7 days and 2046 days in pH 7 and pH 9 solutions. Being a linear optical technique, ATR-IR spectroscopy detects all IR active hydrous species, e.g., bulk and interfacial groups in the pores. Water adsorption, glass network dissolution, and ion exchange occur at surface and interface; thus it is important to understand hydrogen bonding interactions at internal or external interfaces. Owing to the non-centrosymmetric requirement of the second-order non-linear optical process, SFG spectroscopy in general detects only groups at surface (interface) and it is a very powerful technique for studies of interfacial species.[45,87–89]

SFG spectroscopy is a second-order non-linear optical technique in which two laser beams of different frequencies (ω_1 and ω_2) are overlapped temporally and spatially on a sample surface or an interface. The species at the surface/interface are polarized and oscillated to generate the third beam of photons (signal beam) with a frequency equal to the sum of two input frequencies ($\omega = \omega_1 + \omega_2$).[88,89] The technique has been used extensively to study hydrogen bonding interactions of hydrous species at optically flat surfaces and interfaces.[44,45,90] The spectral region of 3000–3600 cm^{-1} generally shows two OH stretch vibrational modes (bands) at ~3200 cm^{-1} and ~3400 cm^{-1}. The former is often attributed to strongly hydrogen-bonded OH stretch mode and the latter is generally assigned to weakly hydrogen-bonded one (see Fig. 5). These spectral features are also referred as "ice-like" (or "solid-like") and "liquid-like" structures, respectively, in the literature.[44,91] The precise assignments of these spectral bands, however, are controversial and still under investigations,[44,90,92–102] and this study will refer to these spectral features as 3200 cm^{-1} band and 3400 cm^{-1} band.

In this study, SFG spectroscopy was first used to study hydrogen bonding interactions on three reference glass samples: polished ISG (uncorroded), fused quartz and porous Vycor. The porous Vycor sample has a porosity of ~28% and pores with an average pore diameter of 4 nm.[20,103] It can be considered as a porous silica sample as it contains ~96 wt.% silica.[104] The alteration layer on corroded ISG is silica-rich (see XPS results) and the use of these reference samples will provide a better understanding of the effects of alteration, chemical composition, and porous structure on the hydrogen bonding interactions of hydrous species on corroded ISG samples. SFG measurements of alteration layer/liquid interface are extremely difficult for long-term corroded samples and in this study, the experiments were performed at different RH values to obtain information on the surface chemistry of the samples. Note that in real applications the corroded samples would be in dry cycles between immersion times. Hydrogen bonding interactions are significantly influenced by SiOH groups and SFG measurements at 0% RH can provide information about SiOH at surfaces/interfaces. The measurements at 40% RH reveal the hydrophobicity/hydrophilicity of the samples while the ones at 90% RH provide information about hydrogen bonding interactions of solid/liquid interface.

The SFG spectra of the reference samples at different RH values are given in Fig. 7. The spectra at 0% RH (Fig. 7a) show no discernible vibrational resonances in the region of 3000–3600 cm^{-1} and the OH stretch mode of the isolated SiOH group appears at ~3740 cm^{-1}. It means that holding samples at 0% RH for >10 h removes a significant amount of physisorbed water molecules from the surface layers and the remaining hydrous species are below the detection limit of the SFG set-up and/or are in centrosymmetric medium. In this condition, the hydrous species are far from each other and the O···HO distance must be larger than 2.3 Å at which the HB interaction is negligible (see Fig. 5).[69,105,106] In the case of
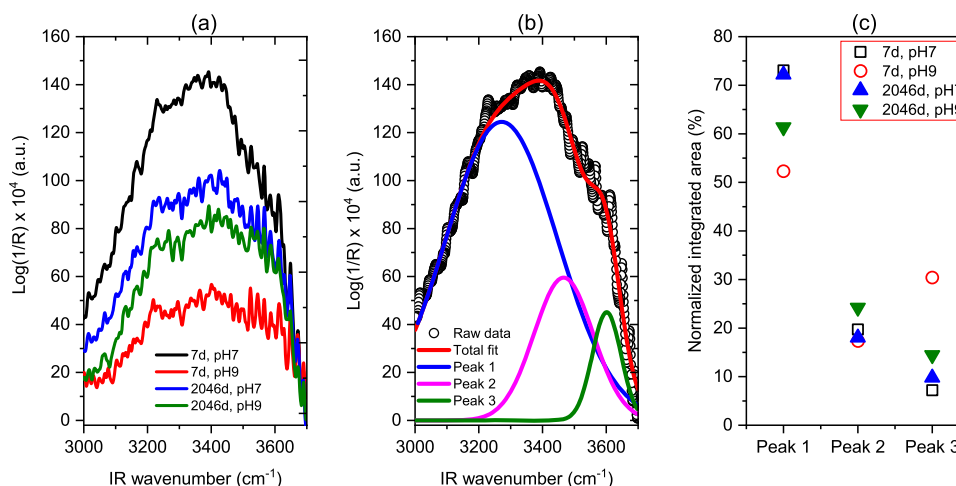
Fig. 6 ATR-IR spectra of hydrous species in the alteration layers formed on ISG samples corroded for 7 days and 2046 days in silica-saturated solutions at pH 7 and pH 9. The spectra were measured at ~37% RH. **a** ATR-IR spectra; **b** Spectral fitting of the spectrum of the sample corroded for 7 days at pH 7; **c** Normalized integrated areas of bands obtained from spectral fittings.

porous Vycor, we could not rule out the possibility that some hydrous species are trapped in closed pores, although we expect such possibility is low. If such species were indeed present, they could have a wide orientational distribution so that their SFG signal may not be collected efficiently in the reflection geometry.[107]

The polished ISG has the lowest free SiOH signal (~3740 cm^{-1}) while the Vycor sample shows the highest SFG intensity. The SFG intensity of free SiOH on Vycor is higher than that of fused quartz and it could be attributed to the higher volume density of SiOH in this sample due to its porosity and surface roughness (see Supplementary Fig. 6 in the SI). Although the lowest SFG intensity of free SiOH on polished ISG could be attributed to the lower OH surface concentration, it should be noted that the orientation of OH groups may also contribute to this lowest intensity.[100] The SFG spectrum of fused quartz at 0% RH is in good agreement with SFG spectra at 0% RH reported in the literature.[100,108]

SFG spectra of polished ISG, fused quartz, and Vycor at 40% RH are given in Fig. 7b. A significant amount of water is adsorbed to the glass surfaces, thus the SFG signals in the 3000–3600 cm^{-1} region show clear spectral features. The spectra at this RH value reveal a dominance of 3400 cm^{-1} band over 3200 cm^{-1} band. The oscillator strength ratio of these bands (A_{3200}/A_{3400}) is given in Fig. 7d. The significantly larger SFG signal at ~3400 cm^{-1} might mean the formation of water clusters around SiOH.[109,110] The A_{3200}/A_{3400} ratio of fused quartz/water vapor interface is significantly larger than those of polished ISG and Vycor; the higher surface density of SiOH groups on the fused quartz facilitates the formation of a more uniform film of strongly hydrogen-bonded "ice-like" water layer.[91,111] Figure 7b also shows that at 40% RH, the sharp peak of isolated SiOH at ~3740 cm^{-1} is shifted to ~3700 cm^{-1} and becomes broader. The presence of this shift has been assigned to the isolated SiOH group that is very weakly hydrogen-bonded; see Fig. 5).[100] The sample surface is not atomically flat and water molecules have only limited access to the isolated SiOH in the topographically depressed region where water access is sterically hindered. This peak has also been attributed to the OH stretch mode of water molecule with its hydrogen atom pointing toward the oxygen atom of siloxane BO group (see Fig. 4e).[65] In the present study, SFG spectroscopy was performed at the air/solid interface, thus a contribution of free-OH stretch mode of molecular water is also possible.[44] The smaller intensity (by a factor of ≥2) and larger peak width of the 3700 cm^{-1} peak at 40% RH in comparison to the intensity and peak width of the 3740 cm^{-1} peak at 0% RH could be partly due to the multiple factors contributing to this peak and IR adsorption by the vapor

phase. In the case of Vycor sample, due to the curvature of the pore surface, isolated SiOH interacting with the oxygen atom of nearby siloxane BO group may also contribute to the SFG signal at ~3700 cm^{-1} (see Supplementary Fig. 5e in the SI).

The SFG spectrum of air/fused quartz at 40% RH (Fig. 7b) shows a dominance of hydrogen-bonded OH stretch signal (3000–3600 cm^{-1}) over the SFG intensity at ~3700 cm^{-1}. This is different from what reported in the work by Liu et al.[108] in which SFG spectrum of silica/air interface at 54% RH still showed a strong OH stretching peak at ~3750 cm^{-1} and very low signal in the 3000–3600 cm^{-1} region in comparison to that at 3750 cm^{-1}. This difference could be due to the different surface preparation methods used in the two studies. The amount of OH groups on silica surface can vary with the surface preparation method due to the nonequilibrium nature of glass.[65,100] Also, a small variance in hydrophobicity of fused silica surface can affect the water adsorption behavior.[108,109,112]

Figure 7c shows SFG spectra of polished ISG, fused quartz, and porous Vycor at 90% RH. SFG intensity is significantly higher than the intensity at 40% RH. The SFG intensity of fused quartz in the 3000–3600 cm^{-1} is significantly larger than that of two other samples. At 90% RH, there can be a thick layer of water formed on fused quartz surface[91] and constructive interference is possible between SFG photons generated at air/water and water/fused quartz interfaces.[100] As a result, enhancement of the hydrogen-bonded OH SFG signal could occur in the 3000–3600 cm^{-1} spectral region. The same can occur on the polished ISG surface. The signal intensity growth is relatively weaker for the porous Vycor glass; this might be due to the filling of internal pores, rather than growth of the uniform layer on the flat surface. The peaks at ~3700 cm^{-1} in the SFG spectra of the polished ISG and fused quartz at 90% RH are narrower than those at 40% RH (see Supplementary Table 4 in the SI). In the SFG spectrum of Vycor at 90% RH in Fig. 7c, the ~3725 cm^{-1} band is extremely small and broad. This must mean that the SiOH groups with very weak HB interactions are significantly decreased upon filling the pores inside.

At 90% RH, the A_{3200}/A_{3400} ratios are larger than those at 40% RH, especially in the case of polished ISG and porous Vycor. Note that the Vycor is porous and silica-rich; thus, its higher ratio in comparison to fused quartz might be attributed to the porous structure of silica-rich surface. The polished ISG has much lower Si-OH density than the silica-rich surfaces (see Fig. 7a) that might lead to a smaller portion of strongly hydrogen-bonded OH groups in the SFG spectrum of the polished ISG surface. The 3400 cm^{-1}

band of Vycor at 90% RH is centered at ~3360 cm^{-1} (see Supplementary Table 4 in the SI), which is somewhat lower than that of vapor/water (~3400 cm^{-1}),[44] polished ISG (~3423 cm^{-1}) and fused quartz (~3393 cm^{-1}). The slightly stronger HBs of these hydrous species in Vycor could be induced by the confined geometry. Owing to the limited space in nanopores, the O⋯HO distance in HBs between water molecules can be shorter (see the Gel298 case in Fig. 4b).

Humidity-dependent SFG analyses of three reference samples (Fig. 7) show that confined geometry of the nano-porous structure, as well as the surface SiOH density can affect the hydrogen bonding interactions in the adsorbed water layers. Figure 8 displays humidity-dependent SFG spectra of hydrous species on the alteration layers on ISG samples corroded for 7 days and 2046 days in silica-saturated solutions at pH 7 and pH 9. The fittings of these spectra are given in the SI (Supplementary Table 4). SFG spectra of polished ISG were also shown for comparison. Recall that ATR-IR spectroscopy detects all IR active hydrous species within the probing volume, while vibrational SFG spectroscopy detects only vibrational modes lying in non-

centrosymmetric medium. Because of that, the number of vibrational modes (number of hydrogen bond populations) and resonant frequencies results from two techniques can be different.

The SFG spectra of corroded ISG samples at 0% RH (Fig. 8a) show no observable hydrogen bonding interactions in the spectral region of 3000–3600 cm^{-1}. Although these samples have alteration layers of different pore sizes (Fig. 3), holding them at 0% RH for a long time removes a significant amount of physisorbed water molecules in open pores in the layers. The hydrogen-bonded hydrous species remaining on alteration layers, as discussed above, are below the detection limit. The SFG intensities of isolated SiOH at ~3740 cm^{-1} on these corroded samples are comparable indicating similar amounts of free isolated SiOH groups lying in the non-centrosymmetric medium within the SFG coherence length from the external surface. The SFG intensity of uncorroded ISG sample at ~3740 cm^{-1} is similar to that of corroded ones while they have higher surface roughness than the uncorroded ISG (see Supplementary Fig. 7 in the SI). It implies that SiOH groups in internal pores of alteration layers also contribute to the measured SFG signal.
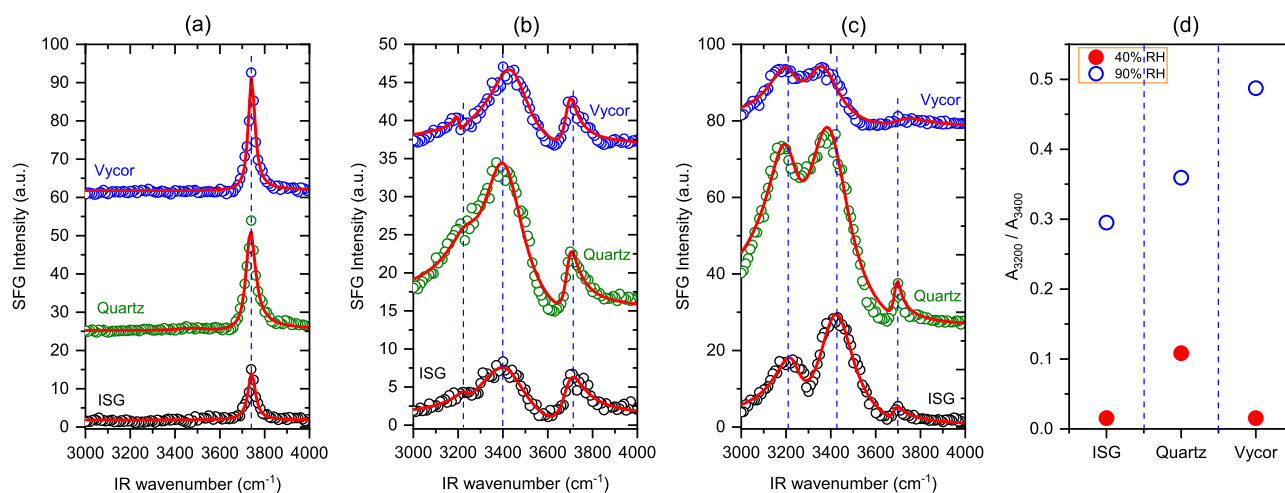

Fig. 7 Humidity-dependent SFG spectra of hydrous species on glass samples at different relative humidity values: 0% (a), 40% (b), 90% (c). The spectra were measured under *ssp* polarization combination and normalized to IR and visible beam intensities. The solid lines are fitted curves obtained from non-linear fittings of SFG spectra. The fit results are shown in Supplementary Table 4 in the SI. The plot in **d** shows oscillator strength ratio of 3200 cm^{-1} band (A_{3200}) and 3400 cm^{-1} band (A_{3400}) at 40 and 90% RH.
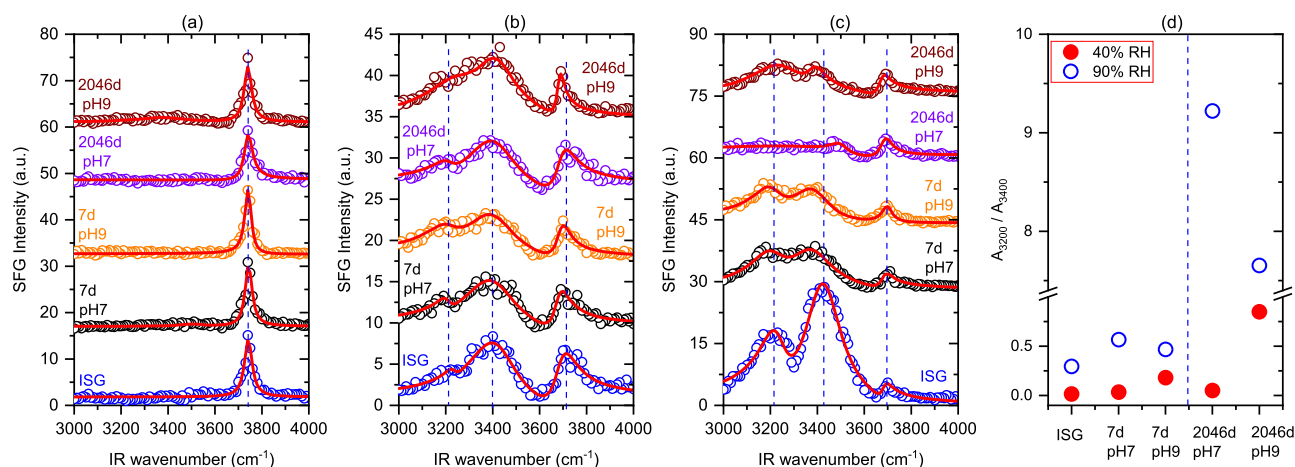

Fig. 8 Humidity-dependent SFG spectra of hydrous species on the alteration layers formed on ISG samples corroded for 7 days and 2046 days in silica-saturated solutions at pH 7 and pH 9: 0% (a), 40% (b), 90% (c). SFG spectra of polished ISG were also shown for comparison. The spectra were measured under *ssp* polarization combination and normalized to IR and visible beam intensities. The solid lines are fitted curves obtained from non-linear fittings of SFG spectra. The fit results are shown in Supplementary Table 4 in the SI. The plot in **d** shows oscillator strength ratios of 3200 cm^{-1} band (A_{3200}) and 3400 cm^{-1} band (A_{3400}) at 40 and 90% RH.

Figure 8b shows the SFG spectra of hydrous species on the alteration layers at 40% RH. The 3000–3600 cm^{-1} spectral region clearly reveals vibrational resonances upon the uptake of water on these corroded samples. This is consistent with results from spectroscopic ellipsometry that show a quick uptake of water into the alteration layer when the relative humidity was increased from 0% RH (Fig. 3). The A_{3200}/A_{3400} ratios of the corroded ISG samples are significantly larger than that of porous Vycor (see Supplementary Table 5 in the SI), which must be due to the difference in surface chemistry, pore sizes and SiOH density between these samples. Figure 4a–d show that Gel298 (gel with smaller pores) has larger portions of shorter (stronger) $O_{water}\cdots H_{water}$ bond and longer (weaker) $O_{water}\cdots H_{silanol}$ bond in comparison to the other two gels with larger pores. Depending on the relative contributions of these HBs to the SFG spectra, the A_{3200}/A_{3400} ratio will vary (see also Supplementary Table 5 in the SI). The 2046-day (pH 9) corroded sample has the A_{3200}/A_{3400} ratio at 40% RH slightly larger than the other corroded samples at the same RH. It means that the portion of ordered hydrous species on this sample is larger than that on other samples. The presence of peaks at ~3700 cm^{-1} could be explained similarly to the case of polished ISG, fused quartz, and Vycor. The SFG spectrum of uncorroded ISG is comparable to that of ISG corroded at pH 7 indicating that the hydrogen bonding interactions on these samples are similar.

The hydrogen bonding interactions of hydrous species in corroded ISG samples at 90% RH are shown in Fig. 8c. At this near-saturation RH, the activity or chemical potential of water vapor is close to that of liquid water; thus, the SFG spectra in this condition could reveal hydrogen bonding interactions that are relevant to the liquid water backfilled pores in the alteration layer. One note of caution is that the pore chemistry might have been altered while the sample was retrieved from the corrosion medium. At 90% RH, most pores in the alteration layers are filled with molecular water as indicated by spectroscopic ellipsometry (Fig. 3). The position of the 3400 cm^{-1} SFG bands of these samples (except the sample corroded for 2046 days at pH 7) is >10 cm^{-1} below that of air/liquid water (see Supplementary Table 4 in the SI) indicating that HBs are stronger in these samples containing nanopores. Figure 8d shows that A_{3200}/A_{3400} ratios of 2046-day-corroded samples are much larger than those of the samples corroded for 7 days and it could be due to the difference in pore network and surface chemistry. As mentioned before, the chemical potential or activity of water vapor at near-saturation humidity is very close to that of liquid water. If the water molecules in the pores are in equilibrium with the vapor phase of water, then the hydrogen bonding interactions detected with SFG could represent those of water molecules filling the pores when the sample is immersed in liquid water. Then, one can infer that the large population of strongly hydrogen-bonded hydrous species (giving a A_{3200}/A_{3400} SFG ratio > 7) might be the characteristic feature of the hydrous species at the stable and very slow corrosion rate in Stage-II. Again, it should be kept in mind that SFG can see only non-centrosymmetric components in the nano-porous medium and that fraction cannot be determined experimentally. The SFG spectrum of uncorroded ISG at 90% RH is very different from that of corroded ones and it is due to the difference in surface chemistry between the samples, as well as porous structure of alteration layers.

The SFG spectrum of the sample corroded for 2046 days at pH 7 is very different from that of other corroded samples, as well as polished ISG. For this sample, the 3200 cm^{-1} band is much broader than other samples (see Supplementary Table 4 in the SI) and the 3400 cm^{-1} band is shifted to 3500 cm^{-1}. It is difficult to conjecture how the small difference in the pore-size distribution of these samples (see Fig. 3) could cause such a drastic contrast in SFG spectra; thus, we speculate that there must be a significant difference in the surface chemistry of pores. There might be a formation of secondary products containing OH groups on this

sample after being corroded for 2046 days in the solution at pH 7. The resonance mode at ~3700 cm^{-1} could be attributed to hydrated isolated SiOH,[100,102] or OH of water with hydrogen atom interacting with the siloxane BO groups (Fig. 4e in the MD section),[65] or free-OH of water at air/thin water layer interface.

The results in this study show a stark difference in the corrosion rate of ISG in silica-saturated solutions at pH 7 and pH 9, as well as an evolution of pore size with corrosion time (see Figs 1–3). The alteration layers contain a significant amount of hydrogen-bonded hydrous species (see ATR-IR results and discussion) and the hydrogen bonding interactions on nano-porous corroded layers are different from reference samples (Figs 7 and 8). However, it is still not obvious what caused such a large difference in the alteration layer thickness in neutral and slightly basic pH conditions. The corrosion processes of ISG glass in silica-saturated solutions at pH 7 and pH 9 are fundamentally similar.[38,54] They both include the leaching of B and cations from the glass network, ion exchange, diffusion of water and other mobile species through the alteration layer, and hydrolysis-condensation reactions.[9] Previous studies showed that the dissolution rate of silica in a solution containing salt is maximum near neutral pH and in this condition the perturbation of surface water is maximized.[113,114] At near neutral pH, the silica surface has a net-negative charge and it attracts hydrated cations to the surface, leading to a more disordered interfacial water structure. This disordered structure is maximized at near neutral pH[114] and it can cause a higher entropy state of the interfacial system and as a result, the dissolution rate is enhanced.[113,114] In the current study, the corrosion solutions contained KCl and were silica-saturated. In these conditions, the dissolution of silicate network is insignificant; however, the alteration layer formed at pH 7 is much thicker than that formed at pH 9. The study by Gin et al.[9] shows that the gel reorganization is a continuous process and it is the key factor contributing to the extremely low water diffusivity (transport) in the alteration layer and therefore limited dissolution of glass. Based on results obtained in this study and the literature, we speculate that the transport of water and mobile species in the alteration layer is slower at pH 9 than pH 7. A slower transport could be possible in an alteration layer containing more smaller pores (Fig. 3) filled with strongly hydrogen-bonded species (Fig. 8d, 90% RH case).

In summary, alteration layers formed on ISG corroded in silica-saturated solutions at pH 7 and pH 9 have a very similar chemical composition as revealed by XPS. Spectroscopy ellipsometry showed that these layers are nano-porous and their pore size evolves with corrosion time in aqueous solutions. Owing to the confined geometry in the layers, various hydrogen bonds between hydrous species were identified by molecular dynamics simulations. Strongly hydrogen-bonded hydrous species are dominant in the nano-porous layers and interfacial hydrogen bonding interactions of these species on alteration layers formed in solutions at pH 7 and pH 9 are different. Further analyses are necessary to link these differences to the mobility of hydrous species and eventually to the glass dissolution rates.

METHODS

Sample preparation

A master block of ISG[53] was provided by MoSci Corp. and was cut into coupons (2 × 2 × 0.1 cm). One large face of each coupon was polished to an optical finish using SiC paper and diamond paste.[38,115] The samples were then cleaned thoroughly using acetone and corroded in aqueous solutions at 90 °C initially saturated with soluble silica as described in refs [38,115]. During the corrosion experiments (7 days and 2046 days), the solution pH was held at 7 ± 0.25 or 9 ± 0.1 by adjusting with a trace amount of 0.01 M KOH and 0.01 M HNO$_3$ solutions periodically. The corrosion solutions at pH 7 and pH 9 contained K$^+$ ions with an initial concentration of 6.8 g/L, and 3.2 g/L, respectively. After retrieving from

aqueous solutions, samples were rinsed quickly with deionized water, dried at 90 °C for 12 h and stored in a desiccator prior to other analyses.

The polished ISG, porous Vycor, and fused quartz were used as reference samples in SFG experiments. The polished ISG was cleaned thoroughly in acetone, ethanol, and water. The Vycor sample (#7930 provided by Corning Inc.) was boiled in a solution of 30% hydrogen peroxide for several hours to remove organic residues and then rinsed thoroughly with DI water. The fused quartz sample was 1 mm thick and one large face was roughened using a glass etching cream (Armour Etch 15-0250) to prevent possible interference in SFG measurement by the signal generated on the backside. This sample was immersed in Nanostrip (commercial piranha, VWR) for at least 12 h and then rinsed thoroughly with DI water. The samples were dried under a nitrogen flow and UV/ozone cleaned for at least 30 min before introducing into the SFG cell. All beakers and tweezers used in the study were cleaned with Liquinox detergent (Alconox, Inc.) and rinsed with a copious amount of DI water.

X-ray photoelectron spectroscopy (XPS)
The elemental depth profiles for Si, O, Na, B, Al, Ca, and Zr in the corroded ISG samples were determined using an XPS instrument (PHI VersaProbe II, Physical Electronics, Inc., Chanhassen, MN, USA) equipped with a monochromatic Al-K_α X-ray source.[49,116] The depth profile of K^+ was not measured in this study, but it is known that K^+ ions in the solution ingress into the alteration layer.[42] The raster sputtering scan over an area of 2×2 mm^2 was performed using a 4 keV Ar$^+$ beam. The depth profile of a SiO$_2$ thin film with a known thickness was measured to determine the sputter rate. The sputtering steps for samples corroded for 7 days (pH 7), 2046 days (pH 7), 7 days (pH 9), and 2046 days (pH 9) were 130, 323, 24, and 48 nm, respectively. During the XPS profile measurements, the crater depths created were 1227, 3488, 220 nm, and 388 nm for 7 days (pH 7), 2046 days (pH 7), 7 days (pH 9), and 2046 days (pH 9), respectively.

Humidity-dependent spectroscopic ellipsometry (SE)
The porosity and pore size of alteration layers formed on ISG samples were characterized using a rotating compensator spectroscopic ellipsometer (Alpha-SE, J.A. Woollam Co.) equipped with a sample cell and an airflow system that allow to control the RH within the cell during the SE measurements. The ellipsometer has a wavelength range of 381–893 nm with a wavelength increment of ~6 nm. The RH value in the cell was monitored using an RH meter with its probe inserted into the cell. The water isotherm was determined for both adsorption and desorption processes. Detailed experimental procedure and data analysis can be found in ref. [40]

Molecular dynamics (MD) simulations of hydrogen bonding interactions of hydrous species in nano-porous silica gels
LAMMPS[117] software was used to perform all MD simulations using a Diffuse Charge Reactive potential initially developed by Mahadevan and Garofalini for the simulation of bulk water[118] and later parameterized for sodium[119] and other elements. Details of the parameters used are given in the previous paper,[119] as well as in the Supplementary Information (SI). Glass structures were initially generated using the above potential by MD-melt-quenching a random glass with a molar composition of 76.8% SiO$_2$, 14.4% Al$_2$O$_3$ and 8.8% CaO. Sodium and boron were not included since they were completely leached out of the alteration layer. The glass composition for MD does not include Zr since the current reactive potential has no parameters for this element and the original Zr content is low (~2 mol%). The MD-melt-quench procedure for this glass has been listed in earlier works[120,121] and consists of increasing the temperature of all atoms in the box to 6298 K for the present system and gradually cooling the system to 1298 K under NVT conditions (constant particle number, volume, and temperature) and then further allowing the system to evolve to the equilibrium density by further cooling to 298 K under NPT conditions (constant particle number, pressure, and temperature). This resulted in a glass with a density of ~2.45 g/cc and conformed to the atomistic structure of glass in terms of its pair distribution functions. The charge scaling method,[122] which has also been used to generate gel structures with other potentials,[123] was used to generate porous gel structures. Thus, the glass boxes were all enlarged and the charges on all species reduced to 20% of their standard values and NVT simulations were carried out for 50 ps. The charges were gradually increased to 30%, 40%, 60%, 80% and eventually 100% with 50 ps at each step. By conducting these NVT simulations at 298, 598, and 998 K, the pore sizes and the
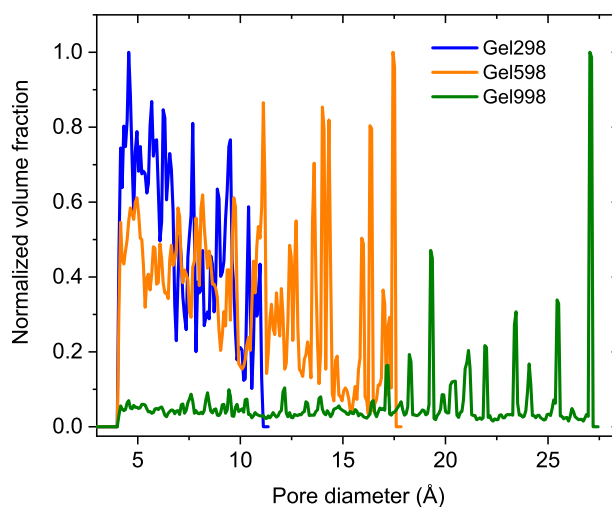
Fig. 9 Relative distribution of pore size in the glasses processed at different temperatures, normalized to the volume fraction of the largest pores. The average pore sizes were 6.95, 9.98, and 17.53 Å for the gels obtained by processing at 298, 598, and 998 K, respectively.

structure of the gels could be controlled. After the charges were scaled to 100% of the original value, a final NPT simulation at different temperatures was done for another 50 ps to allow the system to evolve to its equilibrium density. The resultant nano-porous structures (named Gel298, Gel598, and Gel998 for the 298, 598, and 998 K processed gels, respectively) had pore-size distributions as shown in Fig. 9. The average pore sizes were 6.95, 9.98, and 17.53 Å for the gels obtained by processing at 298, 598, and 998 K, respectively. Thus, higher equilibration temperature led to porous structures with larger sized pores, which are due to higher available thermal energy to rearrange the pore structures.

Following the pore structure generations, water molecules at a density of ~1 g/cm^3 were inserted into the pore areas of the gels using the "regions" feature in the LAMMPS software. The resultant gel-water system was run under NVT conditions for ~2 ns to study the hydrogen bonding interactions and the structural information. We used the pair distribution function to evaluate the distribution of hydrogen bond distances. The first OH peak is around 0.97 Å and extends to a maximum of 1.2 Å and hence the first major peak in the pair distribution beyond 1.2 Å was used as the qualifying criterion for hydrogen bonds. The vibrational density of states (VDOS-spectrum) of hydrous species in gels based on MD results was calculated and VDOS spectra are given in Supplementary Fig. 4 in the SI.

Attenuated total reflection infrared (ATR-IR) spectroscopy
The amount of hydrous species (Si-OH and molecular water) in the alteration layer was measured using a Fourier transform infrared spectrometer equipped with a 20x objective and a Germanium crystal (Bruker Hyperion 3000). The incident angle of the IR beam was 37° and an area of 70×70 μm^2 was examined. Each spectrum was an average of 100 scans and a spectral resolution of 4 cm^{-1} was set for the data collection. The experiments were performed at room relative humidity (~37%). A spectrum of air at room RH was used as the reference.

Vibrational sum frequency generation (SFG) spectroscopy
The hydrogen bonding interactions on the alteration layer were studied using a scanning pico-second sum frequency generation spectrometer (EKSPLA, Lithuania). The SFG measurements were performed using a reflection geometry and more details of the SFG set-up can be found elsewhere.[124] Briefly, a tunable infrared (IR) beam from an optical parametric generator and amplifier (OPG/OPA) pumped by 1064 nm and 532 nm laser beams and a visible (Vis, 532 nm) beam from the pico-second laser were overlapped spatially and temporally on the sample surface to generate a third beam with frequency equal to the sum of IR and Vis frequencies. This SFG beam was then filtered using a monochromator and detected using a photomultiplier tube (PMT). The incident angles of IR and 532 nm beams were 56° and 60° with respect to the surface normal,

respectively. The step scan in SFG experiments was $10\,cm^{-1}$ in the frequency range of $3000–4000\,cm^{-1}$ and each data point was an average of 300 pulses. The SFG spectra were collected with a polarization combination of *ssp* (*s*-polarized SFG, *s*-polarized 532 nm, *p*-polarized IR) and normalized to IR and visible beam intensities to account for the laser power fluctuation. The spectra obtained were then fitted using non-linear curve fittings in Matlab (see the Supplementary Information).

The relative humidity during the SFG measurements was controlled by mixing a dry nitrogen flow and a water vapor-saturated nitrogen flow. Before the collection of SFG spectra of samples at 0% RH, the samples were held in a closed cell with dry nitrogen purging for at least 10 h. At other RH values, the samples were purged with a flow of nitrogen at a specific relative humidity for at least 30 min before the data collection. The dry or humid nitrogen constantly flowed through the cell during the SFG experiments.

DATA AVAILABILITY
The data that support the findings of this study are available from the authors on reasonable request.

REFERENCES
1. Ojovan, M. I. & Lee, W. E. Glassy wasteforms for nuclear waste immobilization. *Metall. Mater. Trans. A* **42**, 837–851 (2011).
2. Gin, S., Ryan, J. V., Kerisit, S. & Du, J. Simplifying a solution to a complex puzzle. *NPJ Mater. Degrad.* **2**, 36 (2018).
3. Ojovan, M. I. & Lee, W. E. in *An Introduction to Nuclear Waste Immobilisation,* 2nd edn (eds Ojovan M. I. & Lee W. E.) 245–282 (Elsevier, 2014).
4. Backhouse, D. J. et al. Corrosion of the International Simple Glass under acidic to hyperalkaline conditions. *NPJ Mater. Degrad.* **2**, 29 (2018).
5. Bates, J. K. & Buck, E. C. Waste glass weathering. *Mater. Res. Soc. Symp. Proc.* **333**, 41–53 (1993).
6. Vienna, J. D., Ryan, J. V., Gin, S. & Inagaki, Y. Current understanding and remaining challenges in modeling long-term degradation of borosilicate nuclear waste glasses. *Int. J. Appl. Glass Sci.* **4**, 283–294 (2013).
7. Frugier, P. et al. SON68 nuclear glass dissolution kinetics: Current state of knowledge and basis of the new GRAAL model. *J. Nucl. Mater.* **380**, 8–21 (2008).
8. Gin, S., Beaudoux, X., Angéli, F., Jégou, C. & Godon, N. Effect of composition on the short-term and long-term dissolution rates of ten borosilicate glasses of increasing complexity from 3 to 30 oxides. *J. Non-Crystalline Solids* **358**, 2559–2570 (2012).
9. Gin, S. et al. Dynamics of self-reorganization explains passivation of silicate glasses. *Nat. Commun.* **9**, 2169 (2018).
10. Zhang, N. et al. Effect of hydrogen-bonding interaction on the arrangement and dynamics of water confined in a polyamide membrane: a molecular dynamics simulation. *J. Phys. Chem. B* **122**, 4719–4728 (2018).
11. Calero, S. & Gómez-Álvarez, P. Hydrogen bonding of water confined in zeolites and their zeolitic imidazolate framework counterparts. *RSC Adv.* **4**, 29571–29580 (2014).
12. Chaplin, M. F. in *Adsorption and Phase Behaviour in Nanochannels and Nanotubes* (eds Dunne Lawrence J. & Manos George) 241–255 (Springer, Netherlands, 2010).
13. Zhu, H., Wang, Y., Fan, Y., Xu, J. & Yang, C. Structure and transport properties of water and hydrated ions in nano-confined. *Channels Adv. Theory Simul.* **2**, 1900016 (2019).
14. Thompson, W. H. Perspective: dynamics of confined liquids. *J. Chem. Phys.* **149**, 170901 (2018).
15. Cerveny, S., Mallamace, F., Swenson, J., Vogel, M. & Xu, L. Confined water as model of supercooled water. *Chem. Rev.* **116**, 7608–7625 (2016).
16. Takahara, S., Sumiyama, N., Kittaka, S., Yamaguchi, T. & Bellissent-Funel, M.-C. Neutron scattering study on dynamics of water molecules in MCM-41. 2. Determination of TRanslational Diffusion Coefficient. *J. Phys. Chem. B* **109**, 11231–11239 (2005).
17. Floquet, N., Coulomb, J. P., Dufau, N., Andre, G. & Kahn, R. Structural and dynamic properties of confined water in nanometric model porous materials (8 Å ≤ ⌀ ≤ 40 Å). *Phys. B: Condens. Matter* **350**, 265–269 (2004).
18. Yamada, S. A., Shin, J. Y., Thompson, W. H. & Fayer, M. D. Water dynamics in nanoporous silica: ultrafast vibrational spectroscopy and molecular dynamics simulations. *J. Phys. Chem. C* **123**, 5790–5803 (2019).
19. Baum, M., Rébiscoul, D., Juranyi, F. & Rieutord, F. Structural and dynamical properties of water confined in highly ordered mesoporous silica in the presence of electrolytes. *J. Phys. Chem. C* **122**, 19857–19868 (2018).
20. Taschin, A., Bartolini, P., Marcelli, A., Righini, R. & Torre, R. A comparative study on bulk and nanoconfined water by time-resolved optical Kerr effect spectroscopy. *Faraday Discuss.* **167**, 293–308 (2013).
21. Bourg, I. C. & Steefel, C. I. Molecular dynamics simulations of water structure and diffusion in silica nanopores. *J. Phys. Chem. C* **116**, 11556–11564 (2012).
22. Mamontov, E. et al. Dynamics of water in LiCl and CaCl2 aqueous solutions confined in silica matrices: A backscattering neutron spectroscopy study. *Chem. Phys.* **352**, 117–124 (2008).
23. Mamontov, E. & Cole, D. R. Quasielastic neutron scattering study of dynamics of CaCl2 aqueous solution confined in Vycor glass. *Phys. Chem. Chem. Phys.* **8**, 4908–4914 (2006).
24. Zhou, T., Bai, P., Siepmann, J. I. & Clark, A. E. Deconstructing the confinement effect upon the organization and dynamics of water in hydrophobic nanoporous materials: lessons learned from zeolites. *J. Phys. Chem. C* **121**, 22015–22024 (2017).
25. Diallo, S. O. Pore-size dependence and characteristics of water diffusion in slitlike micropores. *Phys. Rev. E* **92**, 012312 (2015).
26. Crupi, V., Longo, F., Majolino, D. & Venuti, V. Raman spectroscopy: Probing dynamics of water molecules confined in nanoporous silica glasses. *Eur. Phys. J. Spec. Top.* **141**, 61–64 (2007).
27. Cupane, A., Levantino, M. & Santangelo, M. G. Near-infrared spectra of water confined in silica hydrogels in the temperature interval 365−5 K. *J. Phys. Chem. B* **106**, 11323–11328 (2002).
28. Crupi, V., Majolino, D. & Venuti, V. Diffusional and vibrational dynamics of water in NaA zeolites by neutron and Fourier transform infrared spectroscopy. *J. Phys.: Condens. Matter* **16**, S5297–S5316 (2004).
29. Piletic, I. R., Tan, H.-S. & Fayer, M. D. Dynamics of nanoscopic water: vibrational echo and infrared pump−probe studies of reverse micelles. *J. Phys. Chem. B* **109**, 21273–21284 (2005).
30. Fayer, M. D. & Levinger, N. E. Analysis of water in confined geometries and at interfaces. *Annu. Rev. Anal. Chem.* **3**, 89–107 (2010).
31. Belyanchikov, M. A. et al. Vibrational states of nano-confined water molecules in beryl investigated by first-principles calculations and optical experiments. *Phys. Chem. Chem. Phys.* **19**, 30740–30748 (2017).
32. Ohkubo, T., Gin, S., Collin, M. & Iwadate, Y. Molecular dynamics simulation of water confinement in disordered aluminosilicate subnanopores. *Sci. Rep.* **8**, 3761 (2018).
33. Erko, M., Findenegg, G. H., Cade, N., Michette, A. G. & Paris, O. Confinement-induced structural changes of water studied by Raman scattering. *Phys. Rev. B* **84**, 104205 (2011).
34. Sulpizi, M., Gaigeot, M.-P. & Sprik, M. The silica–water interface: how the silanols determine the surface acidity and modulate the water properties. *J. Chem. Theory Comput.* **8**, 1037–1047 (2012).
35. Li, J.-Y., Wu, Z.-Q., Xu, J.-J., Chen, H.-Y. & Xia, X.-H. Water transport within carbon nanotubes on a wave. *Phys. Chem. Chem. Phys.* **18**, 33204–33210 (2016).
36. Collin, M. et al. Molecular dynamics simulations of water structure and diffusion in a 1 nm diameter silica nanopore as a function of surface charge and alkali metal counterion identity. *J. Phys. Chem. C* **122**, 17764–17776 (2018).
37. Rébiscoul, D. et al. Water dynamics in nanoporous alteration layer coming from glass alteration: an experimental approach. *J. Phys. Chem. C* **119**, 15982–15993 (2015).
38. Gin, S. et al. Origin and consequences of silicate glass passivation by surface layers. *Nat. Commun.* **6**, 6360 (2015).
39. Gin, S. et al. Nuclear glass durability: new insight into alteration layer properties. *J. Phys. Chem. C* **115**, 18696–18706 (2011).
40. Ngo, D. et al. Spectroscopic ellipsometry study of thickness and porosity of the alteration layer formed on international simple glass surface in aqueous corrosion conditions. *npj Mater. Degrad.* **2**, 20 (2018).
41. Lenting, C. et al. Towards a unifying mechanistic model for silicate glass corrosion. *NPJ Mater. Degrad.* **2**, 28 (2018).
42. Collin, M., Fournier, M., Charpentier, T., Moskura, M. & Gin, S. Impact of alkali on the passivation of silicate glass. *npj Mater. Degrad.* **2**, 16 (2018).
43. Du, T. et al. Atomistic origin of the passivation effect in hydrated silicate glasses. *npj Mater. Degrad.* **3**, 6 (2019).
44. Shen, Y. R. & Ostroverkhov, V. Sum-frequency vibrational spectroscopy on water interfaces: polar orientation of water molecules at interfaces. *Chem. Rev.* **106**, 1140–1154 (2006).
45. Nihonyanagi, S., Mondal, J. A., Yamaguchi, S. & Tahara, T. Structure and dynamics of interfacial water studied by heterodyne-detected vibrational sum-frequency generation. *Annu. Rev. Phys. Chem.* **64**, 579–603 (2013).

46. Amma, S.-i., Kim, S. H. & Pantano, C. G. Analysis of water and hydroxyl species in soda lime glass surfaces using attenuated total reflection (ATR)-IR spectroscopy. *J. Am. Ceram. Soc.* **99**, 128–134 (2016).

47. Sheth, N., Luo, J., Banerjee, J., Pantano, C. G. & Kim, S. H. Characterization of surface structures of dealkalized soda lime silica glass using X-ray photoelectron, specular reflection infrared, attenuated total reflection infrared and sum frequency generation spectroscopies. *J. Non-Crystalline Solids* **474**, 24–31 (2017).

48. Sheth, N. et al. Probing hydrogen-bonding interactions of water molecules adsorbed on silica, sodium calcium silicate, and calcium aluminosilicate glasses. *J. Phys. Chem. C* **122**, 17792–17801 (2018).

49. Liu, H., Ngo, D., Ren, M., Du, J. & Kim, S. H. Effects of surface initial condition on aqueous corrosion of glass—A study with a model nuclear waste glass. *J. Am. Ceram. Soc.* **102**, 1652–1664 (2019).

50. Luo, J. et al. Relative abundance of subsurface hydroxyl and molecular water species in silicate and aluminosilicate glasses. *J. Non-Crystalline Solids* **510**, 179–185 (2019).

51. Rébiscoul, D., Bruguier, F., Magnin, V. & Gin, S. Impact of soda-lime borosilicate glass composition on water penetration and water structure at the first time of alteration. *J. Non-Crystalline Solids* **358**, 2951–2960 (2012).

52. Jubb, A. M., Hua, W. & Allen, H. C. Environmental chemistry at vapor/water interfaces: insights from vibrational sum frequency generation spectroscopy. *Annu. Rev. Phys. Chem.* **63**, 107–130 (2012).

53. Gin, S. et al. An international initiative on long-term behavior of high-level nuclear waste glass. *Mater. Today* **16**, 243–248 (2013).

54. Gin, S. et al. The fate of silicon during glass corrosion under alkaline conditions: a mechanistic and kinetic study with the International Simple Glass. *Geochim. et Cosmochim. Acta* **151**, 68–85 (2015).

55. Collin, M. et al. Structure of International Simple Glass and properties of passivating layer formed in circumneutral pH conditions. *NPJ Mater. Degrad.* **2**, 4 (2018).

56. Harris, R. K. & Newman, R. H. 29Si N.M.R. studies of aqueous silicate solutions. *J. Chem. Soc., Faraday Trans. 2: Mol. Chem. Phys.* **73**, 1204–1215 (1977).

57. Tanaka, M. & Takahashi, K. Characterization of silicate complexes in aqueous sodium sulfate solutions by FAB-MS. *J. Solut. Chem.* **34**, 617–630 (2005).

58. Gouze, B., Cambedouzou, J., Parrès-Maynadié, S. & Rébiscoul, D. How hexagonal mesoporous silica evolves in water on short and long term: Role of pore size and silica wall porosity. *Microporous Mesoporous Mater.* **183**, 168–176 (2014).

59. Indris, S., Heitjans, P., Behrens, H., Zorn, R. & Frick, B. Fast dynamics of H2O in hydrous aluminosilicate glasses studied with quasielastic neutron scattering. *Phys. Rev. B.* **71**, 064205

60. Gregg, S. J. & Sing, K. S. W. *Adsorption, Surface Area, and Porosity.* (Academic Press, 1991).

61. Thommes, M. & Cychosz, K. A. Physical adsorption characterization of nanoporous materials: progress and challenges. *Adsorption* **20**, 233–250 (2014).

62. Loizillon, J. et al. In-depth study of coating multimodal porosity using ellipsometry porosimetry in desorption scanning mode. *J. Phys. Chem. C* **123**, 23464–23479 (2019).

63. Kinosita, K. Refractive index and pore structure of acid-leached surface layer of glass. *J. Phys. Soc. Jpn.* **16**, 807–818 (1961).

64. Rimsza, J. M. & Du, J. Nanoporous silica gel structures and evolution from reactive force field-based molecular dynamics simulations. *NPJ Mater. Degrad.* **2**, 18 (2018).

65. Cyran, J. D. et al. Molecular hydrophobicity at a macroscopically hydrophilic surface. *Proc. Natl Acad. Sci.* **116**, 1520 (2019).

66. Kerisit, S. & Liu, C. Molecular simulations of water and ion diffusion in nanosized mineral fractures. *Environ. Sci. Technol.* **43**, 777–782 (2009).

67. Novak, A. Hydrogen bonding in solids correlation of spectroscopic and crystallographic data. In *Large Molecules. Structure and Bonding* (eds Dunitz, J. D., Hemmerich, P., Holm, R. H., Ibers, J. A., Jørgensen, C. K., Neilands, J. B., Reinen, D., Williams, R. J. P.), **18**, 177–216 (Springer, Berlin, Heidelberg).

68. Libowitzky, E. Correlation of O-H stretching frequencies and O-H…O hydrogen bond lengths in minerals. *Monatshefte für. Chem./Chem. Monthly* **130**, 1047–1059 (1999).

69. Wang, H.-W. et al. Vibrational density of states of strongly H-bonded interfacial water: insights from inelastic neutron scattering and theory. *J. Phys. Chem. C.* **118**, 10805–10813 (2014).

70. Pfeiffer-Laplaud, M., Costa, D., Tielens, F., Gaigeot, M.-P. & Sulpizi, M. Bimodal acidity at the amorphous silica/water interface. *J. Phys. Chem. C.* **119**, 27354–27362 (2015).

71. Pfeiffer-Laplaud, M. & Gaigeot, M.-P. Adsorption of singly charged ions at the hydroxylated (0001) α-quartz/water interface. *J. Phys. Chem. C.* **120**, 4866–4880 (2016).

72. Pfeiffer-Laplaud, M., Gaigeot, M.-P. & Sulpizi, M. pKa at quartz/electrolyte interfaces. *J. Phys. Chem. Lett.* **7**, 3229–3234 (2016).

73. Pfeiffer-Laplaud, M. & Gaigeot, M. -P. Electrolytes at the hydroxylated (0001) α-quartz/water interface: location and structural effects on interfacial silanols by DFT-based MD. *J. Phys. Chem. C* **120**, 14034–14047 (2016).

74. Tyrode, E., Rutland, M. W. & Bain, C. D. Adsorption of CTAB on hydrophilic silica studied by linear and nonlinear optical spectroscopy. *J. Am. Chem. Soc.* **130**, 17434–17445 (2008).

75. Gor, G. Y., Huber, P. & Bernstein, N. Adsorption-induced deformation of nanoporous materials—A review. *Appl. Phys. Rev.* **4**, 011303 (2017).

76. Boissière, C. et al. Water confined in lamellar structures of AOT surfactants: an infrared investigation. *J. Phys. Chem. B* **106**, 1032–1035 (2002).

77. Bey Temsamani, M., Maeck, M., El Hassani, I. & Hurwitz, H. D. Fourier transform infrared investigation of water states in aerosol-OT reverse micelles as a function of counterionic nature. *J. Phys. Chem. B* **102**, 3335–3340 (1998).

78. Onori, G. & Santucci, A. IR investigations of water structure in Aerosol OT reverse micellar aggregates. *J. Phys. Chem.* **97**, 5430–5434 (1993).

79. Brubach, J. B. et al. Dependence of water dynamics upon confinement size. *J. Phys. Chem. B* **105**, 430–435 (2001).

80. Brubach, J.-B. et al. Infrared investigation of water encapsulated in non ionic reverse micelles. *J. de. Phys. IV* **10**, Pr7-215–Pr217-218 (2000).

81. Le Caer, S. et al. A trapped water network in nanoporous material: the role of interfaces. *Phys. Chem. Chem. Phys.* **13**, 17658–17666 (2011).

82. Amma, S.-i., Luo, J., Kim, S. H. & Pantano, C. G. Effect of glass composition on the hardness of surface layers on aluminosilicate glasses formed through reaction with strong acid. *J. Am. Ceram. Soc.* **101**, 657–665 (2018).

83. Amma, S.-i., Luo, J., Pantano, C. G. & Kim, S. H. Specular reflectance (SR) and attenuated total reflectance (ATR) infrared (IR) spectroscopy of transparent flat glass surfaces: A case study for soda lime float glass. *J. Non-Crystalline Solids* **428**, 189–196 (2015).

84. Lowenstern, J. B. & Pitcher, B. W. Analysis of H2O in silicate glass using attenuated total reflectance (ATR) micro-FTIR spectroscopy‡. *Am. Mineralogist* **98**, 1660–1668 (2013).

85. Crupi, V., Longo, F., Majolino, D. & Venuti, V. T dependence of vibrational dynamics of water in ion-exchanged zeolites A: a detailed Fourier transform infrared attenuated total reflection study. *J. Chem. Phys.* **123**, 154702 (2005).

86. Behrens, H. & Nowak, M. Quantification of H2O speciation in silicate glasses and melts by IR spectroscopy—in situ versus Quench Techniques. *Phase Transit.* **76**, 45–61 (2003).

87. Wang, H.-F., Velarde, L., Gan, W. & Fu, L. Quantitative sum-frequency generation vibrational spectroscopy of molecular surfaces and interfaces: lineshape, polarization, and orientation. *Annu. Rev. Phys. Chem.* **66**, 189–216 (2015).

88. Bain, C. D. Sum-frequency vibrational spectroscopy of the solid/liquid interface. *J. Chem. Soc., Faraday Trans.* **91**, 1281–1296 (1995).

89. Lambert, A. G., Davies, P. B. & Neivandt, D. J. Implementing the theory of sum frequency generation vibrational spectroscopy: a tutorial review. *Appl. Spectrosc. Rev.* **40**, 103–145 (2005).

90. Urashima, S.-h., Myalitsin, A., Nihonyanagi, S. & Tahara, T. The topmost water structure at a charged silica/aqueous interface revealed by heterodyne-detected vibrational sum frequency generation spectroscopy. *J. Phys. Chem. Lett.* **9**, 4109–4114 (2018).

91. Asay, D. B. & Kim, S. H. Evolution of the adsorbed water layer structure on silicon oxide at room temperature. *J. Phys. Chem. B* **109**, 16760–16763 (2005).

92. Du, Q., Superfine, R., Freysz, E. & Shen, Y. R. Vibrational spectroscopy of water at the vapor/water interface. *Phys. Rev. Lett.* **70**, 2313–2316 (1993).

93. Du, Q., Freysz, E. & Shen, Y. R. Vibrational spectra of water molecules at quartz/water interfaces. *Phys. Rev. Lett.* **72**, 238–241 (1994).

94. Du, Q., Freysz, E. & Shen, Y. R. Surface vibrational spectroscopic studies of hydrogen bonding and hydrophobicity. *Science* **264**, 826 (1994).

95. Sovago, M. et al. Vibrational response of hydrogen-bonded interfacial water is dominated by intramolecular coupling. *Phys. Rev. Lett.* **100**, 173901 (2008).

96. Sovago, M., Kramer Campen, R., Bakker, H. J. & Bonn, M. Hydrogen bonding strength of interfacial water determined with surface sum-frequency generation. *Chem. Phys. Lett.* **470**, 7–12 (2009).

97. Tian, C.-S. & Shen, Y. R. Isotopic dilution study of the water/vapor interface by phase-sensitive sum-frequency vibrational spectroscopy. *J. Am. Chem. Soc.* **131**, 2790–2791 (2009).

98. Nihonyanagi, S. et al. Unified molecular view of the air/water interface based on experimental and theoretical χ(2) spectra of an isotopically diluted water surface. *J. Am. Chem. Soc.* **133**, 16875–16880 (2011).

99. Ostroverkhov, V., Waychunas, G. A. & Shen, Y. R. Vibrational spectra of water at water/α-quartz (0001) interface. *Chem. Phys. Lett.* **386**, 144–148 (2004).

100. Dalstein, L., Potapova, E. & Tyrode, E. The elusive silica/water interface: isolated silanols under water as revealed by vibrational sum frequency spectroscopy. *Phys. Chem. Chem. Phys.* **19**, 10343–10349 (2017).

101. Myalitsin, A., Urashima, S.-h, Nihonyanagi, S., Yamaguchi, S. & Tahara, T. Water structure at the buried silica/aqueous interface studied by heterodyne-detected vibrational sum-frequency generation. *J. Phys. Chem. C* **120**, 9357–9363 (2016).

102. Hore, D. K. & Tyrode, E. Probing charged aqueous interfaces near critical angles: effect of varying coherence length. *J. Phys. Chem. C* **123**, 16911–16920 (2019).

103. Álvarez-Herrero, A., Heredero, R. L., Bernabeu, E. & Levy, D. Adsorption of water on porous Vycor glass studied by ellipsometry. *Appl. Opt.* **40**, 527–532 (2001).

104. Reithmaier, J., Petkov, P., Kulisch, W. & Popov, C. *Nanostructured Materials for Advanced Technological Applications*. (Springer, Netherlands, 2009).

105. Rimola, A., Costa, D., Sodupe, M., Lambert, J.-F. & Ugliengo, P. Silica surface features and their role in the adsorption of biomolecules: computational modeling and experiments. *Chem. Rev.* **113**, 4216–4313 (2013).

106. Libowitzky, E. in *Hydrogen Bond Research* (eds Schuster Peter & Mikenda Werner) 103–115 (Springer, Vienna, 1999).

107. Zhang, L. et al. Nanoporous silica-water interfaces studied by sum-frequency vibrational spectroscopy. *J. Chem. Phys.* **130**, 154702 (2009).

108. Liu, D., Ma, G., Xu, M. & Allen, H. C. Adsorption of ethylene glycol vapor on α-Al_2O_3 (0001) and amorphous SiO_2 surfaces: observation of molecular orientation and surface hydroxyl groups as sorption sites. *Environ. Sci. Technol.* **39**, 206–212 (2005).

109. Casillas-Ituarte, N. N. & Allen, H. C. Water, chloroform, acetonitrile, and atrazine adsorption to the amorphous silica surface studied by vibrational sum frequency generation spectroscopy. *Chem. Phys. Lett.* **483**, 84–89 (2009).

110. Bogdan, A. & Kulmala, M. Effect of acids on water vapor uptake by pyrogenic silica. *J. Colloid Interface Sci.* **191**, 95–101 (1997).

111. Banerjee, J., Kim, S. H. & Pantano, C. G. Elemental areal density calculation and oxygen speciation for flat glass surfaces using x-ray photoelectron spectroscopy. *J. Non-Crystalline Solids* **450**, 185–193 (2016).

112. Isaienko, O. & Borguet, E. Hydrophobicity of hydroxylated amorphous fused silica surfaces. *Langmuir* **29**, 7885–7895 (2013).

113. Dove, P. M. The dissolution kinetics of quartz in sodium chloride solutions at 25 degrees to 300 degrees C. *Am. J. Sci.* **294**, 665–712 (1994).

114. Dewan, S., Yeganeh, M. S. & Borguet, E. Experimental correlation between interfacial water structure and mineral reactivity. *J. Phys. Chem. Lett.* **4**, 1977–1982 (2013).

115. Gin, S. et al. Atom-probe tomography, TEM and ToF-SIMS study of borosilicate glass alteration rim: a multiscale approach to investigating rate-limiting mechanisms. *Geochim. et Cosmochim. Acta* **202**, 57–76 (2017).

116. Ngo, D., Liu, H., Kaya, H., Chen, Z. & Kim, S. H. Dissolution of silica component of glass network at early stage of corrosion in initially silica-saturated solution. *J. Am. Ceram. Soc.* **102**, 6649–6657 (2019).

117. Plimpton, S. Fast parallel algorithms for short-range molecular dynamics. *J. Computational Phys.* **117**, 1–19 (1995).

118. Mahadevan, T. S. & Garofalini, S. H. Dissociative water potential for molecular dynamics simulations. *J. Phys. Chem. B* **111**, 8919–8927 (2007).

119. Mahadevan, T. S., Sun, W. & Du, J. Development of water reactive potentials for sodium silicate glasses. *J. Phys. Chem. B* **123**, 4452–4461 (2019).

120. Mahadevan, T. S. & Du, J. Evaluating water reactivity at silica surfaces using reactive potentials. *J. Phys. Chem. C.* **122**, 9875–9885 (2018).

121. Mahadevan, T. S. & Garofalini, S. H. Dissociative chemisorption of water onto silica surfaces and formation of hydronium ions. *J. Phys. Chem. C.* **112**, 1507–1515 (2008).

122. Beckers, J. V. L. & de Leeuw, S. W. Molecular dynamics simulation of nanoporous silica. *J. Non-Crystalline Solids* **261**, 87–100 (2000).

123. Rimsza, J. M. & Du, J. Structural and mechanical properties of nanoporous silica. *J. Am. Ceram. Soc.* **97**, 772–781 (2014).

124. Barnette, A. L. et al. Selective detection of crystalline cellulose in plant cell walls with sum-frequency-generation (sfg) vibration spectroscopy. *Biomacromolecules* **12**, 2434–2439 (2011).

AUTHOR CONTRIBUTIONS

The scope of the experiment was designed by D.N. and S.H.K. D.N. performed SE and SFG analyses, H.L. carried out XPS depth profiling, H.K. and T.J.Z. involved in IR analysis, S.G. prepared 7-day and 2046-day samples, T.M. and J.D. performed MD simulations. Z.C. carried out AFM analysis. D.N. and S.H.K. wrote the manuscript. All the authors helped on paper editing and approved the final version.

COMPETING INTERESTS

The authors declare no competing interests.

ADDITIONAL INFORMATION

Supplementary information is available for this paper at https://doi.org/10.1038/s41529-019-0105-2.

Correspondence and requests for materials should be addressed to S.H.K.

Reprints and permission information is available at http://www.nature.com/reprints

Publisher's note Springer Nature remains neutral with regard to jurisdictional claims in published maps and institutional affiliations.